Nanoscale

PAPER

View Article Online
View Journal

Cite this: DOI: 10.1039/d5nr04259c

Site-controlled Ge hut wire-based multiple quantum dots with integrated charge sensing capability

Jin Leng,[a,b,c] Fei Gao,[d,e] Yu-Chen Zhou,[a,b,c] Chu Wang,[a,b,c] Hao-Tian Jiang,[a,b,c] Zhi-Tao Wu,[a,b,c] Gang Cao,[a,b,c,f] Jianjun Zhang,[d,f] Hai-Ou Li *[a,b,c,f] and Guo-Ping Guo [a,b,c,f]

Received 9th October 2025,
Accepted 16th March 2026

DOI: 10.1039/d5nr04259c

rsc.li/nanoscale

Scalability represents a fundamental challenge in advancing semiconductor-based quantum computing architectures. Germanium nanowires (NWs) have emerged as a highly promising platform due to their demonstrated high-quality in-plane NW networks. In this study, we demonstrate the fabrication of two distinct sets of multiple quantum dots (QDs) on closely spaced parallel Ge hut wires. Charge sensing is achieved through capacitive coupling between the two sets of QDs. Furthermore, the tunability of both sets of QDs enables mutual detection between dot pairs across arrays. Through systematic gate voltage adjustments, we successfully transition the system configuration from a single quantum dot (SQD) to triple quantum dot (TQD) regimes. We identify edge state impurities in one set of QDs, which may introduce crosstalk effects and potentially hinder qubit detection and manipulation. Through comprehensive analysis and numerical simulations of these edge states, we hope to develop approaches to avoid the formation of such edge state impurities in the future.

1. Introduction

Quantum computing has entered an era where scalability has become a central challenge, particularly in the noisy intermediate-scale quantum (NISQ) regime.[1–7] During this critical phase, the predominant objective involves scaling up the qubit count while maintaining high-quality performance, with particular emphasis on addressing noise robustness and crosstalk to facilitate effective error correction. These fundamental challenges necessitate the development of novel platforms and materials capable of supporting scalable, high-fidelity qubits. Initial investigations on semiconductor quantum dots (QDs) primarily concentrated on III/V material systems, including GaAs QDs,[8–10] InAs nanowires (NWs),[11] and InSb NWs.[12] However, III/V group materials suffer from hyperfine interactions caused by nuclear spins, leading to short coherence times.[8] In contrast, group IV materials such as Si and Ge offer distinct advantages through the utilization of zero-nuclear-spin isotopes (*e.g.*, ^{28}Si and ^{72}Ge) enabled by advanced isotopic purification techniques. In recent years, research on group IV material-based qubits has demonstrated significant advancements.[13–16]

Ge has attracted attention for its unique advantages,[17] including the highest hole mobility[18] and low effective hole mass[19] among semiconductors, enabling progress across various device structures.[17] High-quality, undoped Ge/SiGe planar heterostructures have made possible the realization of QD arrays[20] and high-fidelity qubit gates.[21,22] Ge/Si core/shell nanowires also offer good tunability[23] and spin controllability.[24,25] However, challenges remain, particularly the non-planar growth of Ge/Si core/shell NWs, which complicates device fabrication and hinders large-scale integration.[26]

The recent development of site-controlled Ge hut wires represents a breakthrough in scalable quantum device fabrication.[27] These triangular nanostructures grow deterministically on pre-patterned Si substrates *via* the Stranski–Krastanov mode,[27,28] forming an ordered network ideal for qubit arrays. Their unique triangular cross-section induces strain-mediated heavy-hole dominance,[27,29] significantly prolonging coherence.[30] They also exhibit large *g*-factor anisotropy[31] and strong spin–orbit coupling.[32–34] Recently, a relatively high spin–flip rate has been achieved in double quantum dots (DQDs),[35,36] and an ultrafast and electrically tunable Rabi frequency exceeding 1.2 GHz[37] has been achieved in hole spin qubits.

[a]*Laboratory of Quantum Information, University of Science and Technology of China, Hefei, Anhui 230026, China. E-mail: haiouli@ustc.edu.cn*
[b]*Anhui Province Key Laboratory of Quantum Network, University of Science and Technology of China, Anhui 230026, China*
[c]*CAS Center for Excellence and Synergetic Innovation Center in Quantum Information and Quantum Physics, University of Science and Technology of China, Hefei, Anhui 230026, China*
[d]*Institute of Physics, Chinese Academy of Sciences, Beijing 100190, China*
[e]*Qilu Institute of Technology, Jinan, 250200, China*
[f]*Hefei National Laboratory, Hefei 230088, China*

To further realize scalable qubit array, scalable readout is required. Charge sensing is crucial but remains challenging in nanowire systems. Although demonstrated in Ge/Si core–shell[38,39] and InAs nanowires[40,41] using separate sensor dots, and more recently in single Ge hut wires[42] the capability for mutual capacitive sensing between multiple quantum dots (QD1 can serve as a CS-QD to tune and probe QD2, and conversely QD2 can serve as a CS-QD to tune and probe QD1) – a critical feature for arrayed architectures – has not been achieved. Our work bridges this gap by implementing two parallel Ge hut wires (200 nm spacing) with bidirectionally coupled quantum dots. On the other hand, our device does not require any additional electrode connections between the two sets of nanowires, this bidirectional, mutual charge-sensing capability is an important step toward implementing arrayed quantum architectures.

In this letter, we demonstrate two pairs of multiple QDs formed on adjacent parallel Ge hut wires. These two pairs of QDs are mutually detectable through capacitive coupling. One pair of QDs is utilized as a charge sensing quantum dot (CS-QD) to monitor the other pair. We also achieve fully tunable interdot coupling by adjusting the middle gate voltage, enabling the transformation of one pair of QDs from single quantum dot (SQD) to triple quantum dots (TQDs). Subsequently, we characterize and simulate their properties. Finally, we observe edge-state impurities in the charge sensing measurements of another pair of quantum dots. Through simulation and analysis of the charge stability diagrams associated with the edge-state, we find that it consists of a DQD and a TQD. The emergence of the edge-state leads to crosstalk, which severely affects the properties of the quantum dots. These results demonstrate a scalable quantum dot architecture, which can be further optimized for future quantum computing applications.

2. Device and methods

2.1 Ge hut wire QD device structure

Fig. 1(a) shows an atomic force microscope image of site-controlled Ge hut wires self-assembled on the edge of a patterned Si substrate groove. The black area represents the etched groove, while at the interfaces between the dark and bright regions, there are two parallel Ge hut wires with triangular cross-sections.[27] Based on statistical measurements of cross-sectional images, the Ge hut wires have an average height of approximately 2 nm and an average base width of approximately 35 nm.[27] The mobility of our Ge nanowires is approximately 780 $cm^2\ V^{-1}\ s^{-1}$. Although this value is not particularly high, it is sufficient to fabricate QD devices of good quality with low defect density. Fig. 1(b) presents a scanning electron microscopy image of the fabricated device, where two identical Ge hut wires (200 nm apart) are individually patterned with gate electrodes to form multiple QDs. The left hut wire serves as the measured QD array, while the right functions as a CS-QD, and the two systems are coupled *via* capacitive interaction.

2.2 Fabrication and measurement environment

The QDs are defined by depleting hole gases in the hut wires through three Ti/Pd (5/30 nm) top gates (35 nm width, 70 nm spacing) fabricated by electron-beam lithography. Prior to gate

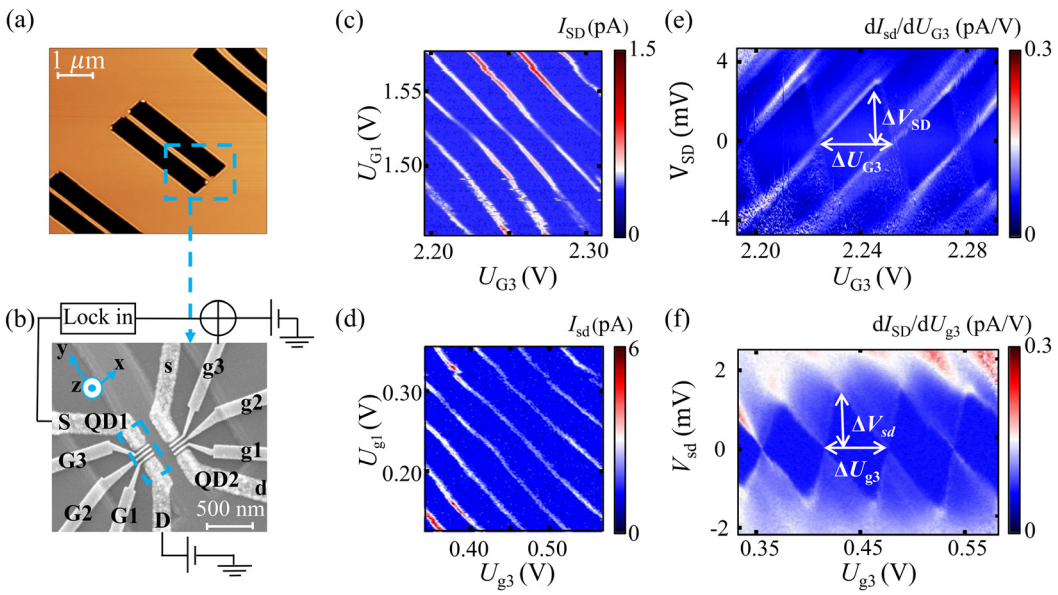

Fig. 1 Device structure and SQD transport measurements. (a) Atomic force microscope images of a pair of parallel pitched-roof Ge NWs grown at the edge of a grooved and patterned Si substrate, with the blue dashed box indicating the location of the QD electrodes prepared. (b) Scanning electron microscopy images of two sets of QD electrodes prepared on the NWs, labeled as uppercase and lowercase letters for the left and right groups of electrodes respectively, with an external charge sensing measurement wiring schematic shown on the outside. (c) and (d) Direct current transport stability diagrams of the QD1 and QD2, respectively. (e) and (f) Coulomb diamond plots of QD1 and QD2, respectively, with the voltage parameters used for lever arm calibration (to convert gate voltage to energy) indicated in the figures.

deposition, a conformal 20 nm Al_2O_3 dielectric was grown by atomic-layer deposition (ALD); this continuous ALD layer provides electrical insulation between the top gates and the underlying conductive structures (including the parallel hut wire on the opposite trench side) and thus prevents accidental shorting. Source and drain contacts are formed by 35 nm thick Pd electrodes. To verify device integrity, completed devices were subjected to electrical tests—gate-to-gate and gate-to-source/drain leakage measurements, across-trench resistance checks, and depletion/transport characterization—and no shorting or abnormal leakage was observed within the relevant bias ranges. All measurements are performed at approximately 20 mK in a dilution refrigerator.

3. Results and discussion

3.1 SQD and Coulomb diamond measurement

Initially, to verify the normal operation of both QDs on each side, we performed transport measurements on them separately. Fig. 1(c) and (d) exhibit characteristic Coulomb blockade oscillations in DC transport for the left and right QDs group (hereafter referred to as QD1 and QD2) respectively, where parallel conductance peaks confirm successful formation of SQDs in both hut wires. The Coulomb oscillations exhibit significant non-linearity and peak splitting as the gate voltages are varied. This behavior is attributed to changes of the left and right gate voltages that alter the QD shape, causing the capacitance matrix to depend on the gate voltages and leading to deviations from a simple linear SQD response. In future device designs we will carry out electrostatic simulations and structural optimizations so that the QD remains stable in a given state over a wider range of gate voltages.

Further characterization through finite bias spectroscopy (Fig. 1(e) and (f)) reveals well-defined Coulomb diamonds, from which we extract the gate lever arms: $\alpha_1 = \frac{e\Delta V_{SD}}{\Delta U_{G3}} = 25.1\,\mathrm{meV\,V^{-1}}$ and $\alpha_2 = \frac{e\Delta V_{SD}}{\Delta U_{g3}} = 22.6\,\mathrm{meV\,V^{-1}}$. These values demonstrate strong electrostatic control over the hole occupation in both QDs systems.

3.2 DQDs measurement and interdot tunneling fitting

Next, in the transition to DQDs, conventional transport measurements are insufficient for resolving the interdot coup-

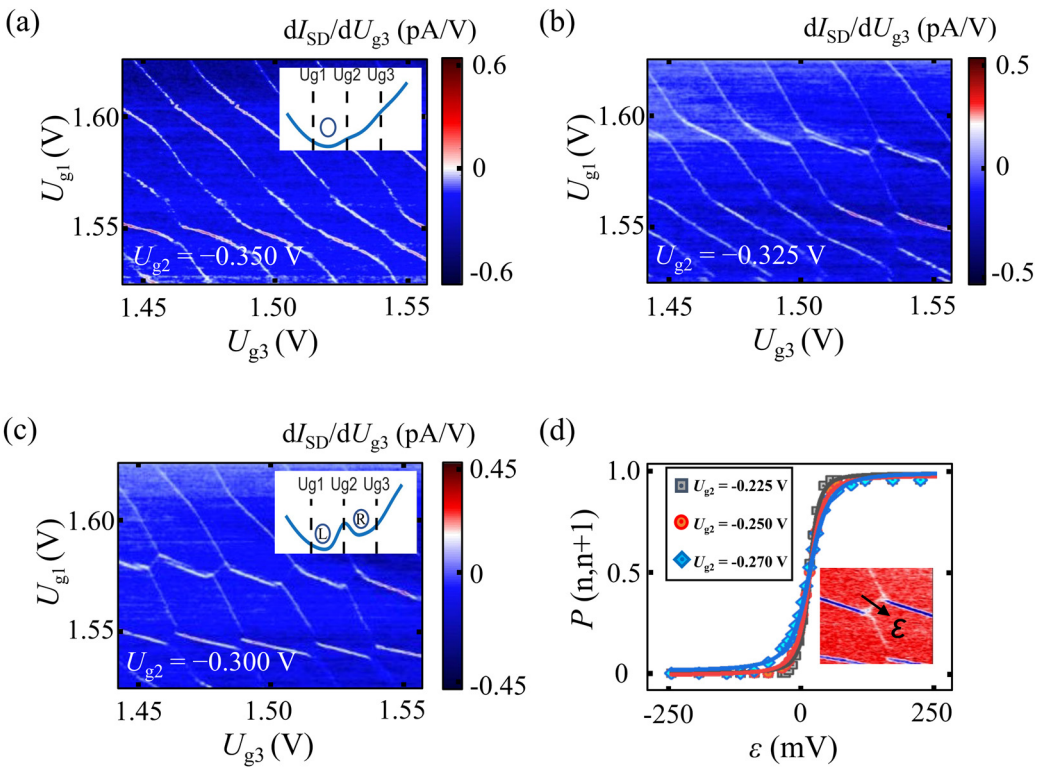

Fig. 2 Coupling control of DQD. (a) Charge sensing phase diagrams measured at U_{g2} = −0.35 V, a series of approximately parallel lines show the features of SQD. The inset in the upper right shows a schematic of the SQD potential well, with the dashed lines indicating the positions of the gates. (b) and (c) Charge sensing phase diagrams measured at U_{g2} = −0.325 V and U_{g2} = −0.300 V, respectively. As the voltage on the middle gate increases, the phase diagram gradually evolves into a honeycomb pattern, indicating the formation of a DQD system. The inset in the upper right of panel (c) shows a schematic of the DQD potential well, with the dashed lines indicating the positions of the gates. The specific locations of the left and right quantum dots are also marked in the schematic. (d) Tunneling current fitting curves at different middle electrode voltages U_{g2}, with data points measured in the ε direction indicated in the inset. When U_{g2} is −0.225 V, −0.250 V, and −0.270 V, the fitted inter-dot coupling strengths are 32.4 μeV, 47.0 μeV, and 69.0 μeV respectively.

ling. Therefore, we used the QD1 as a CS-QD, operating at its Coulomb peak sensitivity point. Due to the electrode capacitance coupling between the QD1 and QD2, when scanning the electrode voltage of the measured QD, CS-QD will deviate from the measurement position. We measured the capacitive coupling between the electrodes of the two pairs of QDs. Then, using compensation method, while adjusting the electrode voltages U_{g1} and U_{g2} of the measured QDs, we change the electrode voltages U_{G1} and U_{G2} of CS-QD together with the electrode voltage of the measured QD, to eliminate the influence of cross-capacitive coupling and obtain a relatively stable measurement area. Details of the charge-sensing measurement method can be found in the SI, "S1 Charge sensing measurement circuit and principle".

As shown in Fig. 2(a–c), by varying the voltage of the middle electrode U_{g2} of the measured QD from −0.35 V to −0.30 V, the QD is gradually tuned from SQD to DQDs. As U_{g2} increases, a small potential barrier forms in the center (see the potential-well schematic in the inset), splitting the well into left and right wells. At U_{g2} = −0.35 V, the phase diagram shows a series of parallel lines, which are characteristic of SQD behavior. At $U_{g2} \geq -0.3$ V, honeycomb patterns emerge, indicating DQD formation. In the DQD regime ($U_{g2} \geq -0.3$ V), we select U_{g2} values of −0.225 V, −0.250 V, and −0.270 V, and extract the interdot coupling strength $2t$ by fitting tunneling current spectra along the detuning ε axis (Fig. 2(d)). We fitted the data to the sensor response model:[38,40]

$$g_s = g_0 + \delta_g \frac{\varepsilon}{\Omega} \tan h\left(\frac{\Omega}{2k_B T_h}\right) \quad (1)$$

where g_0 is the background conductance, ε is the voltage resonance of the charge tunnel line between dots and $\Omega = \sqrt{\varepsilon^2 + (2t)^2}$ is the energy splitting. As ε increases along the arrow direction in the inset of Fig. 2(d), the hole number on the left QD $N(\varepsilon)$ increases from n to $n + 1$. We rescale g_s so that $g_s = P(n,n+1) = N(\varepsilon) - n$. In the fitting formula the parameter $g_0 \approx \delta_g \approx 0.5$, and the hole temperature $T_h \approx 0.1$ K.

The extracted $2t$ values increase monotonically from 32.4 μeV to 69.0 μeV as U_{g2} is varied, demonstrating the electrically tunable nature of the QD coupling.

3.3 TQDs measurement and simulation

Then, we adjust the U_{g1}, U_{g2} and U_{g3} to tune the measured QD into the TQDs regime. As shown by the potential-well schematic in the inset of Fig. 3(e), based on the DQD gate voltages we further increase U_{g2} and simultaneously raise U_{g3}, causing a small potential barrier to form beneath the G3 gate and splitting the potential well in that region into two small potential wells on either side of it. In this case, the QD originally located

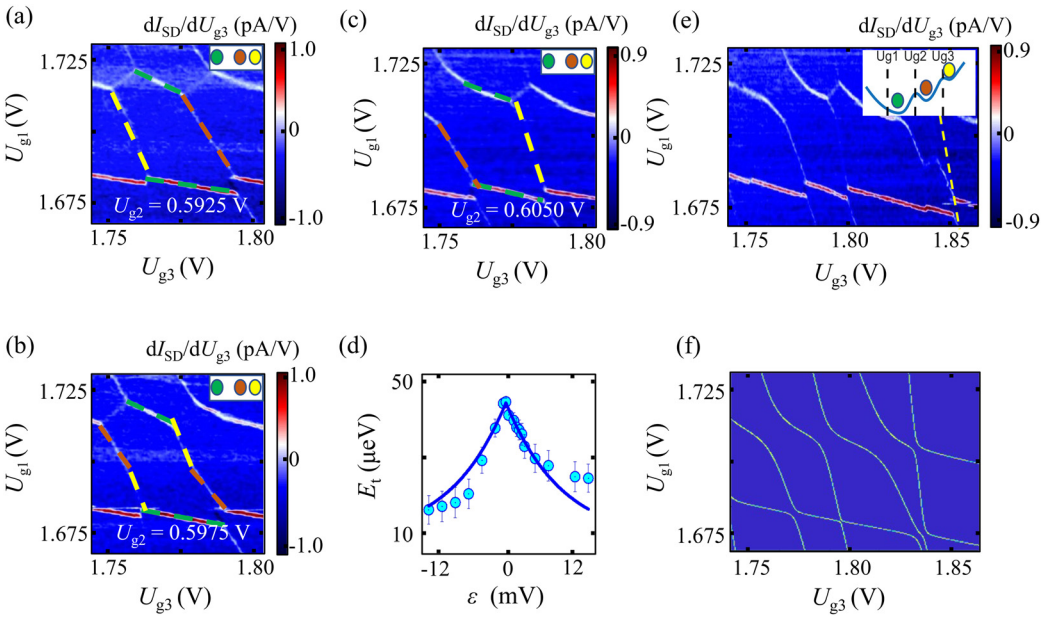

Fig. 3 Measurement and simulation of the TQD phase diagram (a), (b) and (c) Charge sensing diagrams of the TQD system measured at U_{g2} = 0.5925 V, 0.5975 V, and 0.605 V, respectively. The green, brown, and yellow dashed lines indicate the charge transition lines of the left, middle, and right dots. As U_{g2} increases, the chemical potential of the middle dot increases, causing the brown transition line to shift leftward and eventually cross the yellow line. (d) The fitting curve of the indirect tunnel coupling strength E_t between the left and right dot as a function of the middle electrode voltage ΔU_{g2}, with an estimated coupling strength $2t$ of about 31 μeV between neighboring dots. (e) and (f) Comparison between the theoretical simulation and experimental charge sensing diagrams of the TQD system. The dashed lines indicate charge transition lines that were not observed in the experiment due to limitations in measurement accuracy. The inset in the upper right of panel (e) shows a schematic of the TQD potential well, with the dashed lines indicating the positions of the gates. The specific locations of the left (green), middle (brown), and right (yellow) quantum dots are also marked in the schematic.

on the right in the DQD configuration splits into two QDs—the middle (brown) and the right (yellow)—thereby evolving into a TQD system. Fig. 3(a)–(c) track the evolution of charge transition lines for the left, middle and right QDs as U_{g2} increases from 0.5925 V to 0.6050 V. The middle dot's energy shift (brown line) induces an anti-crossing with the right dot (yellow line), revealing indirect coupling through the central dot.

By measuring the tuning effects of each electrode on the QDs, we calculate the capacitance coupling to obtain the charging energy E_{add} = 0.193 meV of the middle dot. The system is modeled through cross-capacitance matrices, yielding the following relationships for the energy shifts:

$$\Delta E_1 = 1.084\Delta U_{g1} + 0.283\Delta U_{g3} \quad (2)$$

$$\Delta E_2 = 0.635\Delta U_{g1} + 0.832\Delta U_{g2} + 1.583\Delta U_{g3} \quad (3)$$

$$\Delta E_3 = 0.172\Delta U_{g1} + 0.720\Delta U_{g2} + 2.663\Delta U_{g3} \quad (4)$$

When the three QD energy levels are tuned to alignment ($E_1 = E_2 = E_3 = E$), a strong indirect tunnel coupling $2t_c$ between the left and right QDs can be measured directly from the anti-crossing curvature in the charge-stability diagram.[43] We define the detuning as $\varepsilon = E_2 - E$, which represents the energy offset of the center QD relative to the sides. Near the region where the three QDs energy levels are aligned, the indirect tunneling coupling $2t_c$ varies with ε according to the relation:

$$E_t = 2t_c = \left(\sqrt{\varepsilon^2 + 8t^2} - |\varepsilon|\right)/2 \quad (5)$$

where $2t$ is the average inter-dot coupling strength between the two neighboring QDs. We fit and obtain that the average inter-dot coupling $2t$ is approximately 31 μeV.

Fig. 3(e) and (f) show that the simulated phase diagrams for TQDs match well with the experimental data, validating our theoretical model.[44] The theoretical model and methods for simulating the TQD phase diagram are described in the SI, "S2. Simulation model of the triple quantum dot phase diagram".

3.4 Edge-state measurement and analysis

Due to the influence of QD shape and the surface electrode structure, the actual position of the wave function may not be at the center of the QD but rather near the edge close to the electrode. For NW QDs, under specific electrode voltage conditions, two groups of edge-state quantum wave functions can form on both sides of the cross-section perpendicular to the NW.[45,46]

As shown in Fig. 4(b), we used the QD2 as the CS-QD to measure the QD1. A complex phase diagram consisting of one

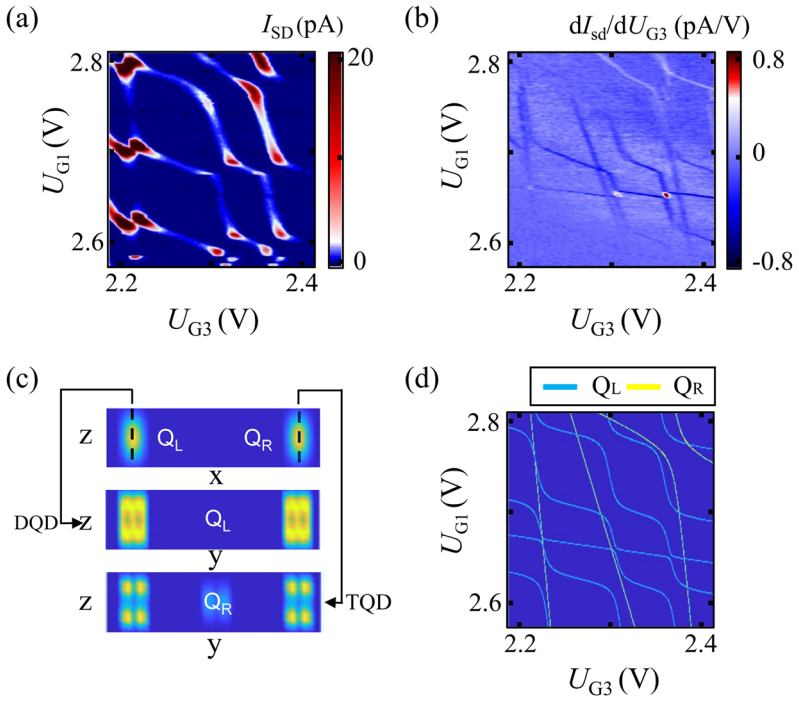

Fig. 4 Measurement and simulation of edge state quantum dots. (a) DC transport measurement phase diagram of edge-state impurities. Due to the limitations of the detection conditions in the DC transport measurement, only one set of DQDs charge filling lines can be detected. (b) Charge induction measurement phase diagram of edge-state impurities, which shows a complex phase diagram consisting of one set of DQDs and one set of TQDs that overlap. (c) By simulating the electric field distribution in NWs and numerically simulating the wave function distribution in NW, three sectional data were displayed separately. Two sets of wave functions are formed on both sides of the NW. In the middle, there is a y–z section distribution of the wave function on one side, arranged in a set of DQDs along the NW. At the bottom is the y–z section distribution of the wave function on the other side, arranged in a set of TQDs along the NW. (d) The phase diagram of edge-state impurities was calculated by numerical simulation of wave functions, and the electric field distribution was adjusted to match the experimental results.

set of DQD and one set of TQD was observed in the charge sensing measurement. However, due to the limitations of DC transport measurements, where V_{SD} = 0.8 mV, as shown in Fig. 4(a), the edge-state impurity phenomenon could not be detected, and only one set of DQD phase diagrams was visible, possibly due to within the applied source–drain bias window, the tunnelling couplings between the TQD energy levels are limited, which significantly inhibits DC current through the TQD.

Because the electrode layout of the sample does not provide sufficient tunability of the edge-state phenomenon, we cannot perform a quantitative analysis of the conditions for edge-state formation; accordingly, we limit our discussion to a qualitative analysis of possible causes. Therefore, in the simulations, a rectangular cross section is used to approximate the triangular cross section (with a wavefunction overlap of up to 97.5%[27]), which is sufficient for a qualitative explanation of this phenomenon. By simulating the electric field distribution in the nanowire using COMSOL we obtained a numerical simulation of the wave function distribution,[47] as shown in Fig. 4(c). In the *z*-direction, the wave function is perpendicular to the sample plane, while the *y*-direction is along the NW direction in the plane, and the *x*-direction is perpendicular to the NW in the plane. In the *x*-direction (*i.e.*, on both sides of the NW in the plane), one set of DQDs and one set of TQDs form, with the difference in the number of left and right dots which may be attributed to the asymmetry of external electrode coverage. By adjusting the electric field distribution, altering the wave function, and calculating the coupling between the dots, the corresponding overlapped DQD and TQD phase diagrams were simulated, as shown in Fig. 4(d), with the left-side DQD having $2t$ = 47 μeV, and the right-side TQD having inter-dot coupling values of $2t_{12}$ = 32 μeV and $2t_{23}$ = 29 μeV

The presence of this edge-state effect may introduce localized impurity dots, potentially leading to crosstalk in qubit control measurements and degradation of qubit coherence. The primary origin of the edge-state effect is the nanowire cross section's large width-to-height aspect ratio (≈20 : 1) and the difference between the electric fields at the edge and at the center. The asymmetry—one side showing a DQD diagram while the other shows a TQD diagram may be caused by: the triangular cross-section, enhanced edge fields due to gate proximity effects, and surface impurities leading to charge accumulation. Further analysis is required to clarify its underlying causes and to develop mitigation strategies, which will aid in optimizing electrode design and identifying more robust intervals for qubit control.

4. Conclusions

In conclusion, we have demonstrated a NW network device so-called site-controlled Ge hut wires. Fully tunable multiple QDs are realized in site-controlled Ge hut wires, and mutual charge sensing is achieved through capacitive coupling between two sets of multiple QDs located on adjacent parallel nanowires. By controlling the electrode voltage on the QDs, we measured, characterized, and simulated the transition of the QD from SQD to TQD. The device can also detect edge states that cannot be detected by transport measurements. Further analysis of this phenomenon in the future can lead to finding better qubit control intervals. Going forward, we plan to benchmark devices with different structural parameters for sensitivity, noise floor, fidelity, sensing operation speed, and stability over time and temperature, in order to quantitatively guide optimization of those structural parameters.

In the Ge hut wires system, due to its strong and tunable spin–orbit coupling,[27,31] fast electrical control of spin state,[37] and suppressed hyperfine interaction,[46] a long coherence time is expected.[35] On the other hand, the possibility of manufacturing NWs of arbitrary length, distance, and arrangement is crucial for achieving scalable spin qubits. Future devices may address the challenges of complex hole qubits and become a potential platform for Majorana qubit implementation.[48–50]

Conflicts of interest

The authors declare no interest conflict. They have no known competing financial interests or personal relationships that could have appeared to influence the work reported in this paper.

Data availability

The data that support the findings of this study are available from the corresponding author upon reasonable request.

Supplementary information (SI) is available. See DOI: https://doi.org/10.1039/d5nr04259c.

Acknowledgements

This work was supported by the National Natural Science Foundation of China (Grant No. 12474490, 62225407, 92565304, 12304225 and 12574552), Quantum Science and Technology National Science and Technology Major Project (Grant No. 2021ZD0302300). This work was partially carried out at the USTC Center for Micro and Nanoscale Research and Fabrication.

References

1 M. Friesen, P. Rugheimer, D. E. Savage, *et al.*, Practical Design and Simulation of Silicon-Based Quantum-Dot Qubits, *Phys. Rev. B:Condens. Matter Mater. Phys.*, 2003, **67**, 121301.
2 S. Gladchenko, D. Olaya, E. Dupont-Ferrier, *et al.*, Superconducting Nanocircuits for Topologically Protected Qubits, *Nat. Phys.*, 2009, **5**, 48–53.

3 B. Douçot and L. B. Ioffe, Physical Implementation of Protected Qubits, *Rep. Prog. Phys.*, 2012, **75**, 072001.
4 A. Chatterjee, P. Stevenson, S. De Franceschi, *et al.*, Semiconductor Qubits in Practice, *Nat. Rev. Phys.*, 2021, **3**, 157–177.
5 I. Siddiqi, Engineering High-Coherence Superconducting Qubits, *Nat. Rev. Mater.*, 2021, **6**, 875–891.
6 N. P. De Leon, K. M. Itoh, D. Kim, K. Mehta, M. L. Noordzij, A. Sammak and M. Veldhorst, Materials Challenges and Opportunities for Quantum Computing Hardware, *Science*, 2021, **372**, eabb2823.
7 X. Zhang, H. O. Li, G. Cao, *et al.*, Semiconductor Quantum Computation, *Natl. Sci. Rev.*, 2019, **6**, 32–54.
8 J. R. Petta, A. C. Johnson, J. M. Taylor, *et al.*, Coherent Manipulation of Coupled Electron Spins in Semiconductor Quantum Dots, *Science*, 2005, **309**, 2180–2184.
9 F. H. L. Koppens, K. C. Nowack and L. M. K. Vandersypen, Spin Echo of a Single Electron Spin in a Quantum Dot, *Phys. Rev. Lett.*, 2008, **100**, 236802.
10 J. Yoneda, T. Otsuka, T. Nakajima, *et al.*, Fast Electrical Control of Single Electron Spins in Quantum Dots with Vanishing Influence from Nuclear Spins, *Phys. Rev. Lett.*, 2014, **113**, 267601.
11 S. Nadj-Perge, S. M. Frolov, E. Bakkers and L. P. Kouwenhoven, Spin–Orbit Qubit in a Semiconductor Nanowire, *Nature*, 2010, **468**, 1084–1087.
12 J. W. G. Van den Berg, S. Nadj-Perge, V. S. Pribiag, *et al.*, Fast Spin-Orbit Qubit in an Indium Antimonide Nanowire, *Phys. Rev. Lett.*, 2013, **110**, 066806.
13 S. G. J. Philips, M. T. Mądzik, S. V. Amitonov, *et al.*, Universal Control of a Six-Qubit Quantum Processor in Silicon, *Nature*, 2022, **609**, 919–924.
14 K. Takeda, A. Noiri, T. Nakajima, *et al.*, Quantum Error Correction with Silicon Spin Qubits, *Nature*, 2022, **608**, 682–686.
15 M. T. Mądzik, S. Asaad, A. Youssry, *et al.*, Precision Tomography of a Three-Qubit Donor Quantum Processor in Silicon, *Nature*, 2022, **601**(7893), 348–353.
16 A. R. Mills, C. R. Guinn, M. J. Gullans, J. R. Petta, *et al.*, Two-Qubit Silicon Quantum Processor with Operation Fidelity Exceeding 99%, *Sci. Adv.*, 2022, **8**(14), eabn5130.
17 G. Scappucci, C. Kloeffel, F. A. Zwanenburg, *et al.*, The Germanium Quantum Information Route, *Nat. Rev. Mater.*, 2021, **6**, 926–943.
18 F. Schäffler, High-Mobility Si and Ge Structures, *Semicond. Sci. Technol.*, 1997, **12**, 1515.
19 R. Pillarisetty, Academic and Industry Research Progress in Germanium Nanodevices, *Nature*, 2011, **479**, 324–328.
20 F. Borsoi, N. W. Hendrickx, V. John, *et al.*, Shared Control of a 16 Semiconductor Quantum Dot Crossbar Array, *Nat. Nanotechnol.*, 2024, **19**, 21–27.
21 N. W. Hendrickx, D. P. Franke, A. Sammak, *et al.*, Fast Two-Qubit Logic with Holes in Germanium, *Nature*, 2020, **577**, 487–491.
22 N. W. Hendrickx, W. I. L. Lawrie, M. Russ, *et al.*, A Four-Qubit Germanium Quantum Processor, *Nature*, 2021, **591**, 580–585.
23 F. N. M. Froning, M. K. Rehmann, J. Ridderbos, *et al.*, Single, Double, and Triple Quantum Dots in Ge/Si Nanowires, *Appl. Phys. Lett.*, 2018, **113**, 073102.
24 F. N. M. Froning, L. C. Camenzind, O. A. H. van der Molen, *et al.*, Ultrafast Hole Spin Qubit with Gate-Tunable Spin–Orbit Switch Functionality, *Nat. Nanotechnol.*, 2021, **16**(3), 308–312.
25 E. Zhuo, Z. Lyu, X. Sun, *et al.*, Hole-Type Superconducting Gatemon Qubit Based on Ge/Si Core/Shell Nanowires, *npj Quantum Inf.*, 2023, **9**(1), 51.
26 C. Jia, Z. Lin, Y. Huang, *et al.*, Nanowire Electronics: From Nanoscale to Macroscale, *Chem. Rev.*, 2019, **119**, 9074–9135.
27 F. Gao, J. H. Wang, H. Watzinger, *et al.*, Site-Controlled Uniform Ge/Si Hut Wires with Electrically Tunable Spin–Orbit Coupling, *Adv. Mater.*, 2020, **32**, 1906523.
28 J. Zhang, M. Brehm, M. Grydlik, *et al.*, Evolution of Epitaxial Semiconductor Nanodots and Nanowires from Supersaturated Wetting Layers, *Chem. Soc. Rev.*, 2015, **44**, 26–39.
29 H. Watzinger, C. Kloeffel, L. Vukusic, *et al.*, Heavy-Hole States in Germanium Hut Wires, *Nano Lett.*, 2016, **16**, 6879–6885.
30 J. Fischer, W. A. Coish, D. V. Bulaev, *et al.*, Spin Decoherence of a Heavy Hole Coupled to Nuclear Spins in a Quantum Dot, *Phys. Rev. B:Condens. Matter Mater. Phys.*, 2008, **78**, 155329.
31 T. Zhang, H. Liu, F. Gao, *et al.*, Anisotropic g-Factor and Spin–Orbit Field in a Germanium Hut Wire Double Quantum Dot, *Nano Lett.*, 2021, **21**, 3835–3842.
32 H. Liu, T. Zhang, K. Wang, *et al.*, Gate-Tunable Spin-Orbit Coupling in a Germanium Hole Double Quantum Dot, *Phys. Rev. Appl.*, 2022, **17**(4), 044052.
33 G. Xu, F. Gao, K. Wang, *et al.*, Hole Spin in Tunable Ge Hut Wire Double Quantum Dot, *Appl. Phys. Express*, 2020, **13**, 065002.
34 T. Zhang, K. Wang, F. Gao, *et al.*, Magnetic Transport Measurements of Spin–Orbit and Hyperfine Interactions in a Ge Hut Wire Double Quantum Dot, *Appl. Phys. Express*, 2021, **14**, 115001.
35 K. Wang, G. Xu, F. Gao, *et al.*, Ultrafast Coherent Control of a Hole Spin Qubit in a Germanium Quantum Dot, *Nat. Commun.*, 2022, **13**, 206.
36 H. Watzinger, J. Kukučka, L. Vukušić, *et al.*, A Germanium Hole Spin Qubit, *Nat. Commun.*, 2018, **9**(1), 3902.
37 H. Liu, K. Wang, F. Gao, *et al.*, Ultrafast and Electrically Tunable Rabi Frequency in a Germanium Hut Wire Hole Spin Qubit, *Nano Lett.*, 2023, **23**, 3810–3817.
38 Y. Hu, H. O. H. Churchill, D. J. Reilly, *et al.*, A Ge/Si Heterostructure Nanowire-Based Double Quantum Dot with Integrated Charge Sensor, *Nat. Nanotechnol.*, 2007, **2**, 622–625.
39 J. H. Ungerer, P. C. Kwon, T. Patlatiuk, *et al.*, Charge-Sensing of a Ge/Si Core/Shell Nanowire Double Quantum Dot Using a High-Impedance Superconducting Resonator, *Mater. Quantum Technol.*, 2023, **3**, 031001.

40 X. Wang, S. Huang, J. Y. Wang, *et al.*, A Charge Sensor Integration to Tunable Double Quantum Dots on Two Neighboring InAs Nanowires, *Nanoscale*, 2021, **13**, 1048–1054.
41 Y. Luo, X. F. Liu, Z. H. Liu, *et al.*, One-Dimensional Quantum Dot Array Integrated with Charge Sensors in an InAs Nanowire, *Nano Lett.*, 2024, **24**, 14012–14019.
42 L. Vukušić, J. Kukučka, H. Watzinger, *et al.*, Single-Shot Readout of Hole Spins in Ge, *Nano Lett.*, 2018, **18**(11), 7141–7145.
43 T. Takakura, A. Noiri, T. Obata, *et al.*, Single to Quadruple Quantum Dots with Tunable Tunnel Couplings, *Appl. Phys. Lett.*, 2014, **104**, 113109.
44 D. Schröer, A. D. Greentree, L. Gaudreau, *et al.*, Electrostatically defined serial triple quantum dot charged with few electrons, *Phys. Rev. B:Condens. Matter Mater. Phys.*, 2007, **76**(7), 075306.
45 B. Voisin, V. H. Nguyen, J. Renard, *et al.*, Few-Electron Edge-State Quantum Dots in a Silicon Nanowire Field-Effect Transistor, *Nano Lett.*, 2014, **14**, 2094–2098.
46 M. F. Gonzalez-Zalba, S. Barraud, A. J. Ferguson, *et al.*, Probing the Limits of Gate-Based Charge Sensing, *Nat. Commun.*, 2015, **6**, 6084.
47 S. Bosco and D. Loss, Fully Tunable Hyperfine Interactions of Hole Spin Qubits in Si and Ge Quantum Dots, *Phys. Rev. Lett.*, 2021, **127**, 190501.
48 F. Peñaranda, R. Aguado, P. San-Jose, *et al.*, Quantifying Wave-Function Overlaps in Inhomogeneous Majorana Nanowires, *Phys. Rev. B*, 2018, **98**, 235406.
49 D. Rainis and D. Loss, Majorana Qubit Decoherence by Quasiparticle Poisoning, *Phys. Rev. B:Condens. Matter Mater. Phys.*, 2012, **85**, 174533.
50 S. Hoffman, C. Schrade, J. Klinovaja, *et al.*, Universal Quantum Computation with Hybrid Spin-Majorana Qubits, *Phys. Rev. B*, 2016, **94**, 045316.

